Optimized emulation of quantum magnetometry via superconducting qubits

N. N. Gusarov [1,2,*] M. R. Perelshtein [1,2,3] P. J. Hakonen [1,2,3] and G. S. Paraoanu [1,2,3]

[1]*Terra Quantum AG, Kornhausstrasse 25, 9000 St. Gallen, Switzerland*

[2]*QTF Centre of Excellence, Department of Applied Physics, Aalto University School of Science, P.O. Box 15100, 00076 Aalto, Finland*

[3]*InstituteQ–The Finnish Quantum Institute, Aalto University, P.O. Box 11000, 00076 Aalto, Finland*

Quantum magnetometry based on adaptive phase estimation allows for Heisenberg precision while avoiding creation and maintenance of complex entangled states. However, the absolute sensitivity is limited by the nonoptimal use of quantum resources provided by multiple-qubit devices and algorithmic realizations of the protocol. Here, addressing both issues, we advance the time-ascending phase estimation protocol by numerical improvements of Bayesian learning, i.e., sequential updating of the field distribution, and optimal exploitation of resources provided by unentangled qubits with limited coherence. Such algorithmic improvements are used to evaluate the absolute sensitivity both on a simulator and by pulsed-transmon experiments conducted on the IBMQ platform, where we take advantage of high coherence time. In addition, we compare the proficiency of separable and entangled states for magnetometry and show that, in practice, separable states provide superior performance. Flux-sensing emulation experiments demonstrate that a sensitivity of $(0.17–1.74)\mu\Phi_0 \, (\sqrt{\text{Hz}})^{-1}$ (where Φ_0 is the flux quantum) for a single-qubit magnetometer and $(0.06–0.65)\mu\Phi_0 \, (\sqrt{\text{Hz}})^{-1}$ for a five-qubit magnetometer can be achieved for slowly oscillating 1–10 kHz magnetic fields, which is comparable to more established experimental platforms for magnetometry.

I. INTRODUCTION

Accurate sensing plays a fundamental role in many scientific studies and industrial applications. Precise measurement of weak magnetic fields is required in brain research [1], biological studies [2], solid-state systems [3,4], and nuclear magnetic resonance [5] and is often performed in challenging environments [6]. Classical magnetometry is usually performed using superconducting quantum interference device (SQUID)–based systems that allow for field sensitivity lower than 1 fT/$\sqrt{\text{Hz}}$ [7], assuming a white-noise limit. However, these devices are operated at 4 K using a bias close to the critical current [8,9], which limits their flux noise to typical values of $(10^{-6}–10^{-7})\Phi_0 \, (\sqrt{\text{Hz}})^{-1}$ [10], where Φ_0 is the flux quantum.

Quantum systems promise to offer a higher precision than classical systems due to quantum resources unavailable in classical measurement settings [11,12]. For instance, quantum phase estimation (QPE) protocols leverage coherence and entanglement [13–15]. In particular, superconducting artificial atoms are promising candidates for accurate magnetic-field measurement since they are easily coupled to magnetic fields using structures similar to SQUID magnetometers. Utilizing QPE implemented on a transmon qubit [16], a flux sensitivity of $10^{-6}\Phi_0 \, (\sqrt{\text{Hz}})^{-1}$ (10 pT/$\sqrt{\text{Hz}}$ field sensitivity) was achieved in Ref. [17]. Nitrogen-vacancy (NV) centers can also leverage QPE for the magnetometer providing a similar flux sensitivity of 10 fT/$\sqrt{\text{Hz}}$ [18].

Recent advances in extending spin coherence in diamonds [19–21], control methodologies [22–25], and hardware [26,27] have improved the performance of quantum magnetometers. Along with hardware improvements, algorithmic improvements may play a crucial role in enhancing the sensing capabilities of these devices. It is now more appreciated that pure algorithmic improvements can provide an advantage to quantum resource utilization (see, for instance, the use of dynamic circuits in quantum computing [28]). Such improvements pave the way towards industrial devices based on quantum phenomena.

However, the ultimate limits of quantum magnetometers that can be built using existing hardware are yet to be explored. In this work we focus on the question of what the best sensitivity is that can be achieved using present-day superconducting qubits and provide an answer by introducing several algorithmic and numerical improvements to existing protocols [17] for quantum magnetometry based on QPE; simulating high-coherence devices and exploring the optimal strategy for magnetometry based on QPE with limited coherence time; extending our approach to a multiqubit setting and evaluating the sensitivity for nonentangled states and entangled Greenberger-Horne-Zeilinger (GHZ) states; emulating magnetometry using state-of-the-art superconducting transmon qubits from the IMB Quantum device (IBMQ), for both single-qubit and multiple-qubit magnetometers; and comparing sensitivity evaluated in our demonstrations to existing magnetometers and fluxmeters and providing a perspective for transmons devices.

For qubits featuring a coherence time of $T_2 \sim 100–200$ μs and a magnetic moment $\mu \sim (10^4–10^5)\mu_B$ [17], we demonstrate that a flux sensitivity of $(0.17–1.74)\mu\Phi_0 \, (\sqrt{\text{Hz}})^{-1}$ and
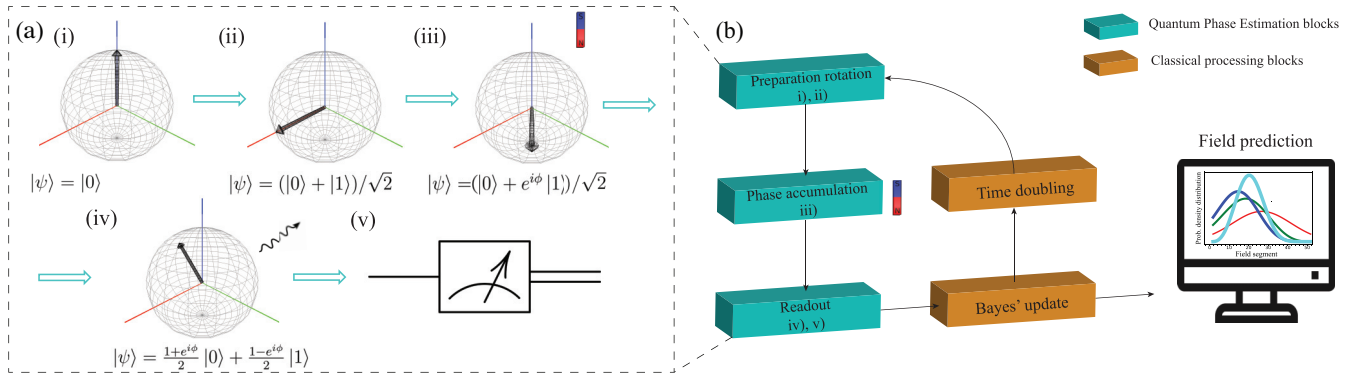
*ngu@terraquantum.swiss

FIG. 1. (a) Bloch sphere representation of operations with a single qubit. The F_c vector, which is parallel to the z axis on the Bloch sphere wave function, evolves as it is shown; the ground-state energy is set to zero. (b) Schematic representation of the Kitaev algorithm. The blue loop repeated k_{max} times corresponds to frames (a i)–(a v). After the process we obtain the field magnitude prediction F_{pr}. The scheme corresponds to Algorithm 1 for a single qubit and Algorithm 2 for multiple qubits.

a field sensitivity of 0.7–7.2 pT/$\sqrt{\text{Hz}}$ can be achieved. We implement our protocol using five unentangled qubits demonstrating a flux sensitivity of $(0.06–0.65)\mu\Phi_0$ $(\sqrt{\text{Hz}})^{-1}$ and a corresponding field sensitivity of 0.3–2.6 pT/$\sqrt{\text{Hz}}$. We also compare this approach with the scheme including entanglement and demonstrate that nonentangled states provide better sensitivity in modern hardware. The given sensitivity values apply at frequencies of the order of approximately $1/T_2 \approx 1$–10 kHz, at which the influence of the $1/f$ noise is already incorporated into T_2. Since our study is based on the Ramsey-type Kitaev algorithm [29] for magnetic-field detection, our protocols are applicable for any qubit system where the accumulated phase is proportional to a constant field value and sensing time, and thus the potential implementations are not limited to superconducting devices.

The paper is organized as follows. In Sec. II we present some general principles of quantum magnetometry based on the Kitaev algorithm and we introduce three algorithmic improvements that lead to a more efficient magnetometry protocol. In Sec. III we discuss the results of magnetometry simulation on IBM Qiskit and for emulation via a single and several superconducting IBM qubits. In Sec. IV we provide a comparison of modern magnetometer platforms and propose and discuss further possible protocol improvements.

II. QUANTUM MAGNETOMETRY USING A SINGLE QUBIT

The core routine used for the measurement of a constant magnetic field via a qubit is the quantum phase estimation algorithm. Here we assume that the magnetic field F_c we are looking for (which we call correct field hereinafter) belongs to a known segment $[F_{min}, F_{max}]$. The algorithm aims at finding F_c in the shortest time and with minimal inaccuracy $\Delta F = |F_{pr} - F_c|$, where F_{pr} is the predicted field value. Interaction between the qubit and the field during a given time causes the qubit to accumulate a phase ϕ. Our magnetometry approach is based on the Kitaev algorithm [29], which includes iterative phase estimation. Therefore, we repeat the phase accumulation at various interaction times t_k, where k is the index of the iteration or step. The qubit-based magnetometer is characterized by an effective magnetic moment μ and co-

herence time T_2 [17]. An iterative phase estimation is a vivid example of hybrid classical and quantum information processing, which is of high interest for quantum computing [30–32].

A. Field estimation

Our magnetic-field-estimation protocol is depicted in Fig. 1. At each kth step of the algorithm, we apply a Hadamard gate to the ground state of the qubit in order to prepare an equal-weight superposition. A qubit prepared in such a state interacts with a magnetic field F for a fixed time t_k, accumulating the phase $\phi(F) = \frac{\mu}{\hbar}Ft_k$. Here we assume that the magnetic field is directed along the z axis on the Bloch sphere, as depicted in Fig. 1. Concluding the protocol with a second Hadamard gate, we perform single-shot readout, obtaining 0 or 1 as an outcome. The probability to measure 1 is given by

$$P_{|1\rangle}^{\text{theor}}[\phi(F)] = \sin^2 \frac{\phi(F)}{2}. \qquad (1)$$

In general, we can repeat the measurement of the qubit's state multiple times n_{rep} and collect the statistics of the binary outcomes.

Since the searching field range is set in advance, we specify the lowest time of interaction t_0 in such a way that the first half of $[F_{min}, F_{max}]$ leads to $|0\rangle$ as the most frequent outcome and the second half leads to $|1\rangle$ [33]. In the case in which t_0 is equal to $\frac{\pi}{2}/(\frac{\mu}{\hbar}F_{mid})$, where $F_{mid} = (F_{min} + F_{max})/2$, the probability function $P_{|1\rangle}[\phi(F)]$ acts as a bijection between $[F_{min}, F_{max}]$ and the $[0, 1]$ interval [34].

Completing the first step, we double the time of interaction at each next step and reduce the span of the search range by a factor of 2. Doubling the interaction time $t_{k+1} = 2t_k$ splits the initial segment $[F_{min}, F_{max}]$ into quarters. For the first and fourth quarters we measure $|0\rangle$ as the most frequent outcome; for the second and third we measure $|1\rangle$. Such a procedure enables a binary searchlike algorithm described in Ref. [34]. The whole estimation routine is shown in Fig. 1(a). The interaction time t_k can be further optimized, as was shown in Ref. [33].

B. Classical and quantum scaling

The operating frequency of the qubit sets certain limits on the control of the device. The resulting sampling rate limits the shortest interaction time between the qubit and the field, which in turn limits t_0 from below. On the other hand, the coherence time T_2 limits the maximal t_k and also the maximal number of steps $k_{\max} \leqslant \log_2(T_2/t_0)$ that can be completed within the coherence time. After completing k steps, the inaccuracy is given by $\Delta F(k) = (F_{\max} - F_{\min})/2^{k+1}$, while the total time of interaction is given by

$$t_{\text{sum}} = \sum_{k=0}^{k_{\max}-1} n_{\text{rep}} t_k = n_{\text{rep}}(2^{k_{\max}} - 1)t_0. \qquad (2)$$

Here we assume that each measurement is performed n_{rep} times. In classical estimation theory, with no quantum resources such as coherence or entanglement, the inaccuracy ΔF can be improved by a value proportional to $t_{\text{sum}}^{-1/2}$, which is referred to as the standard quantum limit (SQL) [14]. However, in the case where the system features quantum resources, such as coherence, the scaling can be improved: $\Delta F \propto t_{\text{sum}}^{-1}$, which is known as the Heisenberg limit (HL) [11]. The number of repetitions n_{rep} enters as a prefactor:

$$\Delta F(t_{\text{sum}}) \propto \frac{n_{\text{rep}}}{t_{\text{sum}}}. \qquad (3)$$

Considering a state-of-the-art single transmon or a NV-center qubit, $k_{\max} \sim 10$ steps are possible. We provide a more detailed analysis in Sec. III A for various devices. If the required precision is not achieved after $k_{\max}$ steps, the algorithm without time doubling (just measuring at $t_{k_{\max}}$) can be continued with standard quantum scaling. In order to push the sensitivity even beyond the coherence time limit (and preserve scaling better than the SQL), it is possible to conduct measurements with interaction times $t_k > T_2$ and investigate the algorithm performance in comparison with the standard quantum limit strategy.

C. Bayesian learning

In order to extract the value of the magnetic field from the outcomes, Bayesian learning can be applied. Bayesian learning is a way of acquiring information from a set of given events (e.g., measured binary values) and their probabilities, given by Eq. (1). The important feature of this approach is that it can self-correct occasional errors due to saving data from previous measurements in the form of a normalized probability density function (PDF).

We discretize the $[F_{\min}, F_{\max}]$ range into an equidistant grid with a grid step δF. This step is given by the initial field range and the number of steps that we can complete, i.e., it is the desired field inaccuracy.

Each step of the algorithm, which is defined by the interaction time t_k and the number of measurements n_{rep}, allows us to renew the PDF via the Bayes formula

$$P(F_{\text{i}}|b_k) = \frac{P(F_{\text{i}})P_{b_k}(F_{\text{i}})}{\sum_{j=1}^{N} P(F_{\text{j}})P_{b_k}(F_{\text{j}})}. \qquad (4)$$

Such a PDF tells us what the probability to estimate F_{i} is in the case in which we measure b_k on the kth step of the algorithm.
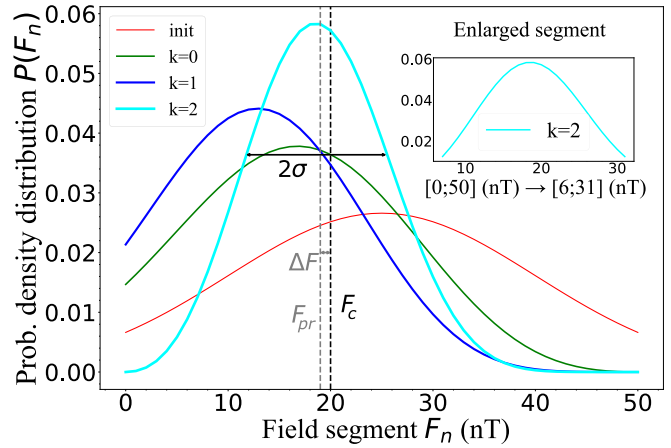

FIG. 2. Initial Gaussian PDF (see Sec. II C 1) and steps of the PDF evolution guided by Eq. (4). Here we show only the first two steps to illustrate the evolution of the distribution. Each step is taken after n_{rep} measurements for each t_k and the most frequent outcome is chosen. Finally, at the $k = 2$ step the algorithm removes half of the initial [0; 50] nT segment and makes δF_{new} half as large as at the previous steps (see the inset).

Here we repeat the measurement n_{rep} times and b_k is the most frequent outcome. The $P(F_{\text{i}})$ is the current PDF and $P_{b_k}(F_{\text{i}})$ is the conditional probability to measure b_k if the qubit interacts with the field F_{i}. Such a conditional probability can be defined by Eq. (1) or refined as we show below.

We assume that the current prediction of the algorithm's F_{pr} is given by F_{i} with the highest probability value. Since we adopt the continuous function description, we consider the half-width of the PDF σ, which is ideally reduced by factor of 2 at each step. We refer to the $\pm\sigma$ segment around F_{pr} as the peak (see Fig. 2 for illustration).

In order to process the results of the probability field update, we introduce several numerical techniques that facilitate the algorithm stability.

1. Initialization

The PDF $P(F_{\text{i}}|b_k)$ evolves via Eq. (4) at each step of the protocol. Ideally, we aim to achieve a narrow Gaussian peak at the end of the algorithm. As was shown in Ref. [33], the initial uniform distribution $P(F) = 1/N$ introduces distortion to Bayesian learning and complicates the field evaluation. Therefore, we initialize the PDF with a wide half-width Gaussian distribution

$$P(F) = \frac{1}{\sqrt{2\pi\sigma_{\text{init}}^2}} \exp\left(-\frac{(F - F_{\text{mid}})^2}{2\sigma_{\text{init}}^2}\right), \qquad (5)$$

where $\sigma_{\text{init}} = (F_{\max} - F_{\min})/2$ (see Fig. 2).

2. Adaptive numerical processing

The PDF half-width σ cannot be smaller than the grid spacing δF, since the PDF peak should include several grid points. However, if the initial grid is not fine enough, we face problems with the numerical processing due to the lack of discretization. In order to avoid such an issue, we increase the number of discretization points δF as necessary: We change

the grid by refining the δF to be half as wide $\delta F_{\text{new}} = \delta F / 2$. In order to keep the amount of points on the segment the same, we get rid of a half of the values F_i each time δF decreases such that the remaining values form a segment symmetric with respect to the currently predicted field F_{pr}.

Essentially, we expand (zoom in on) the necessary segment and process only such a redefined part. The protocol is illustrated in Fig. 2. We initiate the zoom in when the half-width σ becomes close to δF: $\sigma \leqslant 10 \times \delta F$. The coefficient can be varied according to the initial segment. As a result, we always get enough points under the peak during all k_{max} steps of the execution. Therefore, ΔF and σ are not limited by the segment split δF.

The challenge we encounter is that the algorithm can redefine the segment in the "wrong direction", which does not contain the correct field value F_c. However, in such a case the PDF will reveal the error at the next step since the PDF loses its Gaussian-fitting form. Tracking such anomalies, we shift the enlarged segment along the field values for a half of the new segment's length before the next step; such manipulations return the segment range to the position where it contains F_c.

3. Rescaling the probability due to decoherence

The conditional probability for the Ramsey sequence defined in Eq. (1) can be refined in the following way:

$$P_{|1\rangle}^{\text{modif}}[\phi(F)] = \left\{ P_{|1\rangle}^{\text{theor}}[\phi(F)] - 0.5 \right\} e^{-t_k/T_2} + 0.5. \quad (6)$$

Here $P_{|0\rangle,|1\rangle}^{\text{modif}}$ is noticeably different from $P_{|0\rangle,|1\rangle}^{\text{theor}}$ when t_k is of the same order as T_2. Thus, we involve this modification in such cases only.

However, with all the above-mentioned numerical techniques, our magnetometry procedure is not free from errors. We call an error an event when the most frequent (according to the probability distribution) b_k is not measured: 0 (1) instead of 1 (0). While the half-width of the PDF, σ, does not contain information errors, we introduce the sensitivity

$$A = \max(\Delta F, \sigma) \sqrt{t_{\text{sum}}}, \quad (7)$$

with units of T $(\sqrt{\text{Hz}})^{-1}$, which reflects the real performance of the protocol: The lower the value, the better the magnetometer. Sensitivity provides information not only on the final difference between the desired and obtained field magnitude, but also on the time spent to reach the result. Additionally, via sensitivity A we can monitor if the inequality $\Delta F < \sigma$ is satisfied: In the case in which it is not satisfied at step k, the sensitivity A starts to grow (time increases, inaccuracy $\Delta F > 0$ is nearly constant, and the half-width σ decreases). This is an indicator of an error at step k.

D. Pseudocode

The routine for a magnetic-field measurement via a single qubit, which is illustrated in Fig. 1, is expressed in pseudocode in Algorithm 1. First, to simplify the notation let us introduce several auxiliary functions. The function $\text{PDF}_{\text{init}}(F_{\text{min}}, F_{\text{max}})$ returns an initial Gaussian distribution corresponding to Eq. (5). The function $\texttt{new\_out}(t_k)$ stands for the interaction with quantum hardware: Corresponding to Fig. 1, it includes initialization, control, interaction with the magnetic field, and measurement, the result of which it returns. The function

$\texttt{Bayes}(\text{PDF}, b_k)$ is implemented according to Eq. (4). The functions $\texttt{find\_peak}(\text{PDF})$ and $\texttt{find\_sigma}(\text{PDF})$ return F_{pr} and σ, respectively. The function $\texttt{enlarge}()$ is described in Sec. II C 2. When appropriate, it updates F_{min} and F_{max} and divides δF by 2.

Algorithm 1. Single-qubit magnetometry algorithm.

```
t_0 ← π/2/(μ/ℏ  F_mid) # Initial time of
    interaction
PDF ← PDF_init(F_min, F_max) # Initial PDF
t_k ← t_0 # Current time of interaction
for k ← 0 to k_max − 1 do
    for i ← 1 to n_rep do
        out ← out + new_out(t_k) # Measurement
            capture
    end
    b_k ← round(out/n_rep) # Most frequent outcome
    PDF ← Bayes(PDF, b_k) # Bayesian update
    t_k ← 2  t_k # Increasing the time of
        interaction
    σ ← find_sigma(PDF) # Current half-width
    if σ ≤ 10  δF then
        enlarge() # Enlarge field segment
    end
end
F_pr ← find_peak(PDF) # Field prediction
ΔF ← |F_c − F_pr| # Resulting inaccuracy
```

III. SIMULATION AND EMULATION OF MAGNETOMETRY

By adjusting the parameters, qubit-based magnetometry methods can be deployed using various platforms. One of the goals of this work is to benchmark magnetometry algorithms utilizing devices with relatively high coherence time. IBM superconducting devices feature a coherence time of approximately 100 μs, and an open-source software framework QISKIT [35] enables the operation of small quantum devices, including manipulation of quantum states using microwave pulses.

Utilizing the QISKIT framework, we *simulate* magnetometry protocols with perfect qubits and under the effect of adjustable thermal relaxation noise. We test the algorithms using actual superconducting devices that are controlled by microwave pulses, which we call *emulation* hereinafter. While IBM qubits do not allow for the flux tuning, we emulate the interaction with the magnetic flux via the Ramsey interferometry protocol. We keep the number of control pulses the same as it would be in an actual field sensing, encoding the field magnitude in the frequency detuning of the Hadamard gate that is used to prepare a initial superposition. In such a configuration, the qubit starts to accumulate the phase in the same manner as it would be affected by an external magnetic field.

Further, we expand the magnetometry algorithm to multiqubit schemes. In Sec. III C we propose a straightforward magnetometry protocol for several nonentangled qubits coupled to the same field. Instead of complicated entanglement, which is challenging to prepare, we "share" the information among qubits classically. While the scaling is not improved

using that scheme, the absolute sensitivity, as we show below, benefits from this approach.

A. Parameters

We consider regular transmon qubits as a platform for the quantum magnetometer. Such devices can feature an effective flux sensing area of 500 μm^2 resulting in a magnetic moment of $\mu \sim 10^5 \mu_B$ [17,36,37]. We would like to emphasize that the magnetic moment of this artificial atom is directly proportional to the area of the sensing loop, L^2 if L is the loop size. Assuming the $1/f$ flux noise from spin flips of magnetic impurities located near the loop to be the main source of decoherence [38], the noise strength increases linearly with the loop size L, which degrades the flux resolution by a factor of $\sqrt{L}$ [17]. The degradation comes due to the decrease in the dephasing time [39]. The corresponding magnetic-field resolution still improves with increasing loop size as $L^{-3/2}$.

In the simulations we set $T_1 = T_2 = 200$ µs. For experimentally realistic values of the magnetic moment μ and of the relaxation or coherence times T_1 and T_2, we refer to Refs. [17,40]. This set of parameters leads us to the final inaccuracy in the magnetic-field estimation of approximately 10^{-12} T. We analyze the algorithm through the simulation of detection of magnetic fields in the range of $[0; 50]$ nT, requiring the initial time of $t_0 \approx 40$ ns, which is implementable using state-of-the-art transmon qubits [41]. The total number of steps is therefore equal to $k_{max} = 13$.

We start by varying the interaction time at each step approaching T_2 in 13 steps. Utilizing QISKIT, we construct a circuit by applying a Hadamard gate and applying the operator that is responsible for the interaction with a field F_c, i.e., adds a required phase that depends on the correct field value $R_z(\phi) = \exp(-i\phi\sigma_z)$, where σ_z is a Pauli matrix. Thus, we set the simulation parameters so they correspond to the correct field value. Such an approach is clearly relieved of any hardware errors and thus it is used as a baseline for sensitivity.

Considering the current error rate, we analyze the number of repetitions required in given settings and set it to $n_{rep} = 41$. We do not estimate the required fidelity of the qubit readout procedure directly, but rather utilize an estimation of the whole performance success rate (see Appendix A). The number of repetitions, however, is a tunable parameter and should be calibrated for a particular hardware.

B. Magnetometry emulation using a single superconducting qubit

We emulate the magnetometry process by detuning the frequency of the first Hadamard gate instead of coupling magnetic flux to the qubit, since IBM qubits are not flux tunable. In order to estimate the sensitivity, we utilize the QISKIT PULSE framework using a single-qubit IBMQ-Armonk quantum processing unit (QPU). We operate superconducting qubits, preliminary calibrating pulses, qubit frequency ν_0, and readout parameters (via $I - Q$ quadratures) before each execution. We also monitor the coherence time T_2.

The whole protocol of a single step of the quantum phase estimation algorithm is shown in Fig. 3(a). We alter the frequency of the first H pulse, required for the first Hadamard gate ν^{signal}: We add a frequency offset $\delta\nu$ to the qubit frequency ν_0. The detuning is set to

$$\delta\nu = \nu^{signal} - \nu_0 = \frac{1}{2\pi}\frac{\mu}{\hbar}F. \qquad (8)$$

For a flux-sensitive transmon device we have $\mu = \hbar d\omega_{01}/dB$, where ω_{01} is the qubit's transition frequency and B is the real magnetic field. Since in this work the magnetometry is only emulated, we call the effective magnetic field F to avoid confusion with the real B. When this is done at the kth step, we let the free oscillations evolve during the time t_k. The qubit oscillates in the equatorial plane at an angular speed of $2\pi \times \delta\nu$. Importantly, during these oscillations the setting lacks coupling of the flux noise due to the absence of pickup (SQUID) loops in the IBM qubits. However, charge noise, quasiparticle tunneling, critical current noise, and resonator-induced dephasing affect the qubit. The oscillations are terminated after t_k with another (not-detuned) H pulse.

For a single-qubit emulation we use IBMQ-Armonk with $\nu_0 = 4.97$ GHz. The H gates are Gaussian enveloped pulses, cut at $\pm 3\beta$, where β is the half-width of the envelope form; $\delta\nu \sim 1$ MHz. The measurements are performed using a resonator at 6.99 GHz frequency.

Using the IBMQ-Armonk processor ($T_1 \approx 160$ µs and $T_2 \approx 250$ µs) and $n_{rep} = 41$, we achieve a scaling of σ according to the HL, as shown in Fig. 3(c) for a single qubit. Assuming $\mu = 10^5 \mu_B$, we evaluate the final sensitivity to be $A = 0.7$ pT/$\sqrt{Hz}$, while the last measurement is performed at 183 µs, as shown in Fig. 3(d) for a single qubit. At large delay times for the final steps, the half-width and sensitivity begin to increase as the decoherence scrambles the dynamics of the qubit, preventing new information about the field distribution from being learned from measurements. The sensitivity obtained from simulation of a single transmon ($T_2 = 200$ µs) is $A = 0.48$ pT/$\sqrt{Hz}$, which is better than that from the emulation due to errors at the penultimate step that the algorithm tries to self-correct. This sensitivity is obtained at a frequency corresponding to approximately $1/T_2 \approx 1$ kHz, where the influence of $1/f$ noise is already included in T_2. For the single-qubit demonstration, the algorithm shrinks the PDF to the actual F_c with a 95% success rate. One can easily increase this rate by increasing the number of measurements n_{rep}, but that leads to worse sensitivity A since a longer total time is required. The total time of interaction is $t_{sum} \sim 5$ ms.

Since the goal of this work is to estimate the best sensitivity that can be obtained using state-of-the-art devices, we consider a fast reset approximately equal to 100 ns [42], a fast H gate approximately equal to 50 ns, and a fast measurement approximately equal to 250 ns [43]. Thus, a distinct majority of the total time of the magnetometry will be contributed by the total interaction time t_{sum}. In the case when the magnetic moment μ lies in the $(10^4$–$10^5)\mu_B$ range, we obtain a sensitivity $A = 0.7$–7.2 pT/$\sqrt{Hz}$.
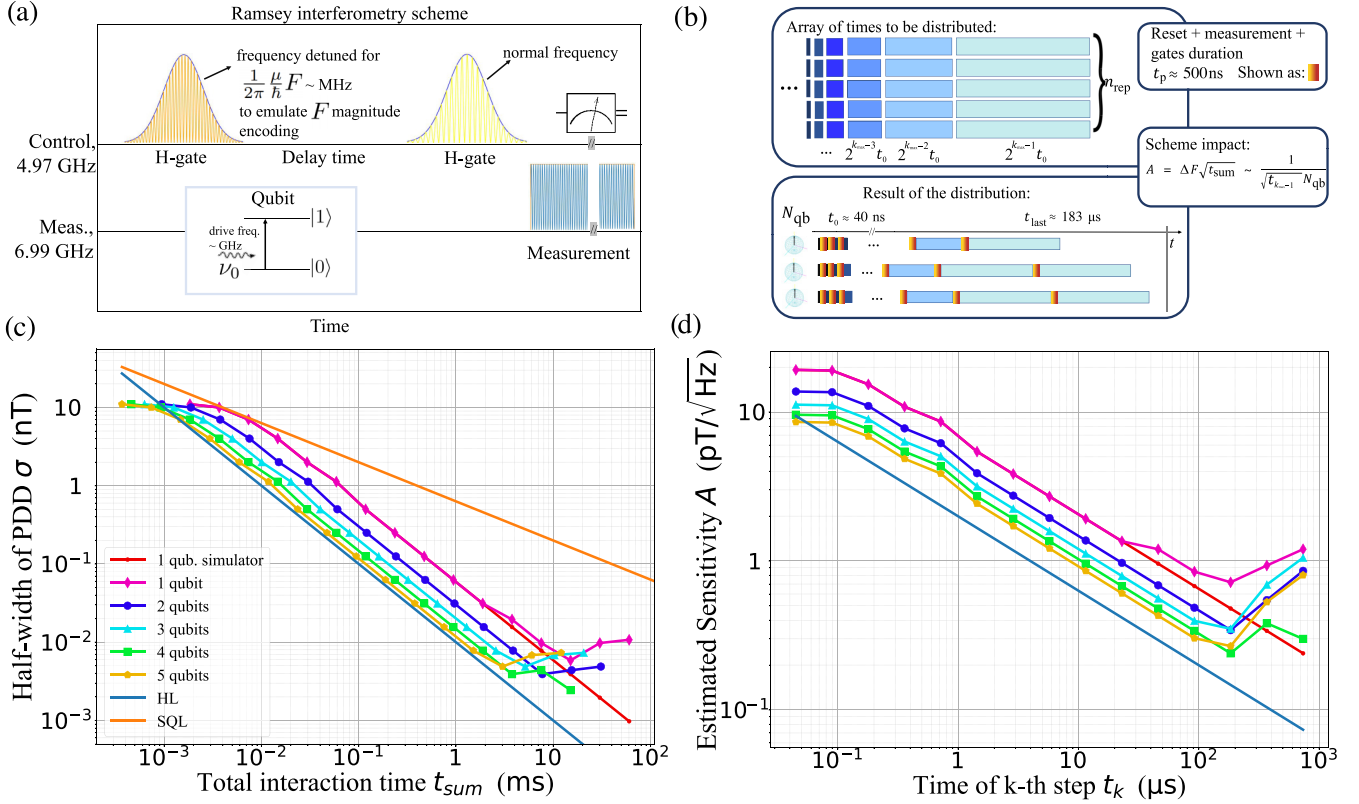
FIG. 3. (a) Ramsey interferometry scheme on IBMQ-Armonk with two Gaussian-enveloped signals: detuned H gate, delay time, H gate, and measurement at another frequency channel. The same scheme was used for the IBMQ-Lima device. In contrast to the case when the qubit accumulates the phase due to continuous interaction with the field, we encode the field value in the first pulse frequency shift. By adding an artificial delay we accommodate for the interaction time, which contributes to the total sensing time. (b) Illustration of the multiqubit algorithm (described in Algorithm 2) that assigns a single measurement with t_k to multiple qubits. The scheme is depicted for $N_{qb} = 3$ qubits given $n_{rep} = 5$ measurement repetitions. According to the inequality (B1), such an assignment allows us to minimize the total magnetometry time t_{sum}. (c) Half-width of the resulting field distribution σ as a function of total time t_{sum}. As expected, σ follows the Heisenberg limit perfectly on the noiseless simulator (red curve). During the demonstrations using actual devices—IBMQ-Armonk for a single qubit and IBMQ-Lima for multiple qubits—we observe some perturbations caused by self-correction of the algorithm. With the increase of N_{qb}, the half-width σ improves by a factor of $\sqrt{N_{qb}}$, as expected. The HL and SQL scalings are also depicted in dark blue and orange, respectively. (d) Estimated sensitivity A for the last five steps of the demonstrations in (c). The inset depicts the theoretical and demonstrated dependences of the obtained sensitivity on the number of qubits at the last (14th) step of the algorithm. For the single-qubit emulation, we assume $\mu = 10^5 \mu_B$ and reach a sensitivity of $A = 0.7$ pT/$\sqrt{\text{Hz}}$ on the last step with a 183 µs interaction (delay) time. The simulation with the perfect qubit provides $A = 0.48$ pT/$\sqrt{\text{Hz}}$, which is better due to errors at the penultimate step that the algorithm tries to self-correct. For the five-qubit emulation, we reach $A = 0.26$ pT/$\sqrt{\text{Hz}}$. The sensitivity values apply at frequency corresponding to approximately $1/T_2 \approx 5$ kHz. Due to the self-correction of the algorithm, the sensitivity and inaccuracy ΔF may grow, which is expected for last steps of the algorithm, where the delay time is close to the coherence time $t_k \sim T_2$, e.g., five-qubit sensitivity is worse than the four-qubit sensitivity.

C. Multiqubit algorithm

1. Separable-state scheme

A significant challenge of the magnetometry protocol considered is the maximization of the success rate of the algorithm; in order to shrink the probability distribution to the correct field value, many repetitions of measurements n_{rep} may be required. However, an increase in the number of measurements leads to the increase of the total algorithm runtime, which reduces the resulting sensitivity. Here we propose to utilize multiple unentangled qubits, each of which takes part in the measuring of the magnetic field with a fixed interaction time at all k_{max} steps.

The whole scheme is depicted in Fig. 3(b) and described in pseudocode in Algorithm 2. In such a setting we redistribute $k_{max} \times n_{rep}$ single-shot measurements across multiple qubits. We can control each qubit in parallel by assigning the measurements according to Algorithm 2 and avoiding the creation of complex quantum states. In contrast to the single-qubit algorithm (Algorithm 1), the multiqubit scheme requires parallel qubit operation. First, we assign times to measure (jobs) to each qubit according to the distribution algorithm using tthe function `assign_job`$(N_{qb}, n_{rep}, k_{max})$. We conduct all assigned measurements in parallel [function meas $\leftarrow$ `undertake_meas`()] and obtain the raw results. For each step k, we obtain the most frequent result via

most_frequent(meas, k). Then, similarly to the single-qubit algorithm, we perform a Bayesian evolution of the initial PDF through k_{max} steps.

Algorithm 2. Multiqubit-qubit magnetometry algorithm.

```
assign_job(N_qb, n_rep, k_max) # Job assignment for
  qubits
meas ← undertake_meas() # Sensing using given
  qubits
PDF ← PDF_init(F_min, F_max) # Initial PDF
for k ← 0 to k_max − 1 do
    b_k ← most_frequent(meas, k) # Preparing
      results
    PDF ← Bayes(PDF, b_k) # Bayesian update
    σ ← find_sigma(PDF) # Current half-width
    if σ ≤ 10  δF then
      | enlarge() # Enlarge field segment
    end
end
F_pr ← find_peak(PDF) # Field prediction
ΔF ← |F_c − F_pr| # Resulting inaccuracy
```

Based on Sec. II C, all the k_{max} measurements can be processed in arbitrary order; we collect corresponding bits, order them, and update the probability distribution. The total magnetometry time t_{sum} consists of an interaction time and a qubit manipulation time t_p, including reset, gates, and readout duration. Reset takes approximately 100 ns [42], gates take approximately 50 ns, and readout takes approximately 250 ns [43], resulting in a total manipulation time of $t_p \sim 500$ ns. We divide all $k_{max} \times n_{rep}$ measurements in chunks of size n_{rep} and, starting from t_0, we assign a single measurement with the shortest t_k to an available qubit. Once all the measurements with t_k are completed, the algorithm will start measurements with t_{k+1}.

For the multiqubit experiments we use the IBMQ-Lima device (see the device description in Appendix D). For the separable-state scheme, we estimate the resulting sensitivity by distributing the measurements among multiple qubits using Algorithm 2. The results of these demonstrations are presented in Figs. 3(c) and 3(d) for one to five qubits. For all executions the final measurement was performed at 183 μs. The final sensitivity achieved is 0.72 pT/$\sqrt{Hz}$ for a single qubit and 0.26 pT/$\sqrt{Hz}$ for a five-qubit scheme with the magnetic moment taken as $\mu = 10^5 \mu_B$. This sensitivity relates to the frequency of the decoherence rate of approximately $1/T_2 \approx 10$ kHz. If the magnetic moment $\mu = (10^4 – 10^5)\mu_B$, the sensitivity obtained for five qubits becomes 0.3–2.6 pT/$\sqrt{Hz}$. For the nonentangled multiqubit scheme (see Appendix B for details), the sensitivity A scales as

$$A = \Delta F \sqrt{t_{sum}} \propto \frac{1}{\sqrt{t_{k_{max}-1}} N_{qb}}. \tag{9}$$

2. Entangled-state scheme

Our scheme can be improved by using entangled qubits, for example, the well-known GHZ states [11,44]. In general, using an entangled system is known to improve the quantum

phase estimation [45–48], i.e., K correlated probes enhance the sensitivity leading to Heisenberg scaling in a number of probes $1/K$ [11,49]. In that case

$$A = \Delta F \sqrt{t_{sum}} \propto \frac{1}{\sqrt{t_{k_{max}-1}} N_{qb}}, \tag{10}$$

while the scaling in time of the last steps remains the same but the prefactor improves with an increase in the number of qubits.

Here we implement GHZ states in the IBMQ-Lima device by coupling the target qubit with other qubits via controlled-NOT (CNOT) gates. The final sensing state with N_{qb} qubits is given by

$$|\psi_{GHZ}\rangle = (|0\rangle^{\otimes N_{qb}} + |1\rangle^{\otimes N_{qb}})/\sqrt{2}. \tag{11}$$

Despite the device connectivity, which does not allow for coupling all qubits to one, the circuit is easily transpiled by QISKIT [50].

The comparison of sensitivities between separable and GHZ states is presented in Fig. 4. While the sensitivity is improved by a factor of $\sqrt{N_{qb}}$, as expected, the GHZ states become incoherent in significantly shorter times than the separable states [50]. This explains the improved sensitivity at shorter times as well as the inability to preserve the Heisenberg scaling long enough to beat the sensitivity obtained using a separable state. The best sensitivity for entangled scheme is observed for a five-qubit GHZ state, 1.7 pT/$\sqrt{Hz}$ for $\mu = 10^5 \mu_B$.

The resulting dependence of the best obtained sensitivity on the number of qubits is demonstrated in Fig. 5, where separable-state and entangled-state schemes follow the predicted law; however, the sensitivities for the GHZ-based scheme lie above the separable-state results. This suggests that it is possible to partially entangle qubits within optimal subsets of the system, optimizing the overall sensitivity; such a scheme is also known to improve the results of Ramsey spectroscopy [51,52]. This approach is a subject left for future research.

IV. COMPARISON OF DIFFERENT MAGNETOMETER TYPES AND PERSPECTIVES

According to the emulations on IBMQ-Armonk, a single transmon is theoretically able to provide a field sensitivity of $A = 720$ fT/$\sqrt{Hz}$. Another important metric is the flux sensitivity, which is calculated taking into account the sensing area [17]; the flux sensitivity obtained in the demonstration is $A_\Phi = 175 n \Phi_0 (\sqrt{Hz})^{-1}$.

The comparison between existing transmon-based magnetometers, potentially improved ones, and most promising state-of-the-art platforms is shown in Fig. 6(a). The SQUIDs (1), optically pumped systems (2), and NV centers (3) are shown in blue, while our transmon scheme is shown in orange circles.

Regarding magnetometry using flux-tunable superconducting qubits, there are two ways to enhance the sensitivity through hardware improvements. (i) One way is to increase the number of qubits N_{qb}, which are not entangled but can all sense the magnetic field. In diamond magnetometer, such an approach is widely used for a field sensing [54]. In the case
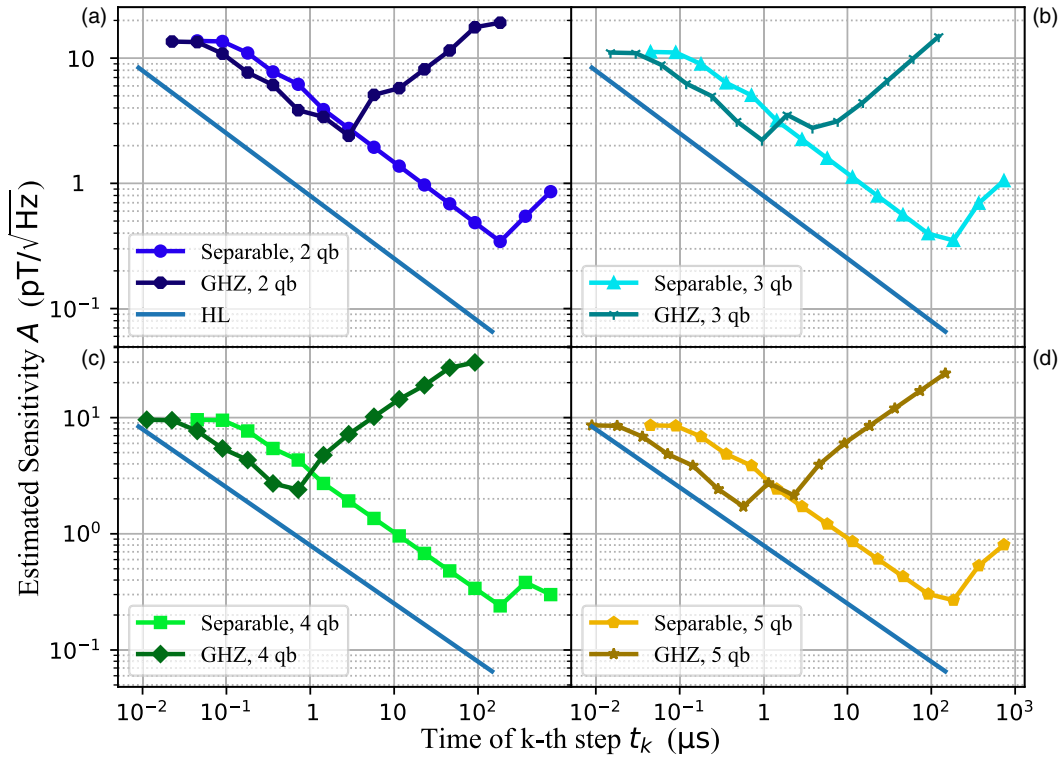
FIG. 4. Comparison of sensitivities for separable-state and GHZ-state multiqubit schemes for (a) two qubits, (b) three qubits, (c) four qubits, and (d) five qubits. Here $\mu = 10^5 \mu_B$. While GHZ states improve the sensitivity by a factor of $\sqrt{N_{qb}}$ compared to the separable-states case, the Heisenberg scaling in delay time is the same for the two schemes (depicted in blue). The GHZ states ideally offer better sensitivity but they are extremely hard to preserve; the separable-state scheme is affected by decoherence after the 13th step, the GHZ already becomes worse after 7th–8th steps.

of superconducting circuits, a uniform field can be directed to each of the transmons using, e.g., a flux-current-flux transformer as shown in Fig. 6(b) and distributing jobs according to the presented protocol. Using the flux-distribution transformer, we keep the input flux the same in each sensor, not
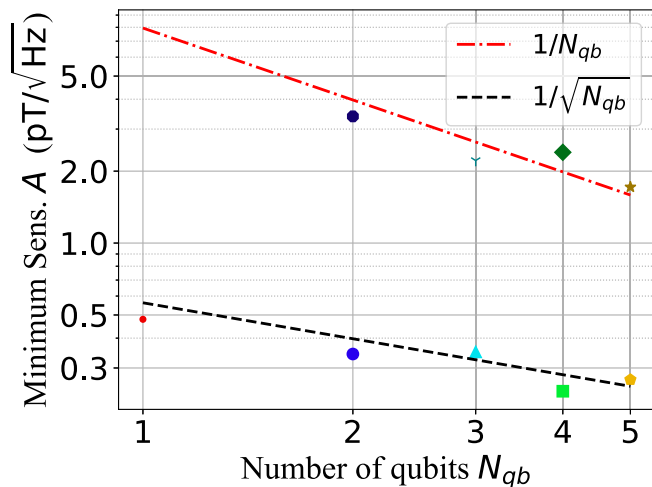

FIG. 5. Best sensitivities for separable and GHZ states from Fig. 4. While the GHZ- and separable-state sensitivities follow the corresponding dependences on the number of qubits $N_{\rm qb}$ (see the legend), the minimum absolute sensitivities for the GHZ-based scheme are an order of magnitude worse than for the separable scheme.

spoiling the flux sensitivity A_Φ. By employing 100 unentangled qubits, both flux and field sensitivities can be improved by an order of magnitude. Here it is not necessary for qubits to be identical, as the magnetic moments can be calibrated and accounted for during measurements. (ii) The increase in coherence time T_2 improves the sensitivity. In our work we assume $T_2 \sim 200$ μs, but an increase up to 1 ms would help to achieve field sensitivity of approximately 10 fT/$\sqrt{\rm Hz}$ and a flux sensitivity of approximately $1 n\Phi_0 (\sqrt{\rm Hz})^{-1}$ for 1-kHz signals. Such coherence times were achieved for fluxonium qubits [55] and 500 μs was achieved for transmons [56], so we expect the 1-ms threshold to be reached in the near future.

Direct current SQUID magnetometers, which are widely used commercially, provide a 0.1 fT/$\sqrt{\rm Hz}$ field sensitivity [7] with the flux noise limited to $(0.1–1.0)\mu\Phi_0 (\sqrt{\rm Hz})^{-1}$. Such devices require cryogenic temperatures of 4 K, which is easier to maintain compared to the dilution refrigerator needed for transmons.

Optically pumped, atomic, magnetometers (OPMs), feature 0.1 fT/$\sqrt{\rm Hz}$ field sensitivity approximately 1 cm^3 in size [53]. However, such a large size makes them impractical for spatially precise measurements. Reducing their size to that of transmons results in a sensitivity of 100 fT/$\sqrt{\rm Hz}$. However, such ambient-temperature OPMs are promising alternatives to cryogenic devices.

Nitrogen-vacancy centers in diamonds have been carefully studied as magnetometers [18,19,57–59] and can provide a sensitivity of approximately 100 fT/$\sqrt{\rm Hz}$ [60]. In order to
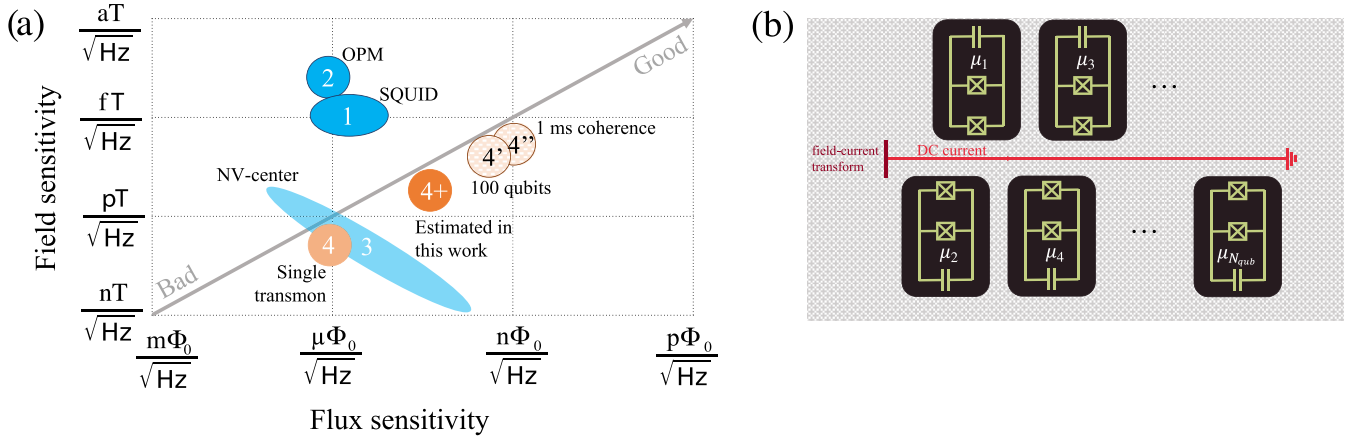
FIG. 6. (a) Field and flux sensitivities of SQUIDs (1) from Ref. [7], optically pumped devices (2) from Ref. [53], NV centers (3) from Ref. [18], and transmon-based magnetometers (4) from Ref. [17]. Since NV centers are sensitive to the field rather than to a flux we consider the sensing areas of such magnetometers and calculated flux sensitivity. We compare them to results estimated in this paper (4+) with the algorithmic improvements described in Sec. II C, and potential sensitivities when the number of qubits is increased up to 100 (4') and increasing T_2 up to 1 ms for each qubit (4''). (b) Schematic representation of a possible multiqubit magnetometer setup, where the qubits are not entangled and are all controlled independently. The measurements are distributed between qubits according to Algorithm 2. The flux transformer (vinous) is a device that delivers the same flux to all qubits. Such a scheme can be used for multiqubit emulation (4') and (4'').

estimate the flux sensitivity, we consider the characteristic sensing area to be in the range of 1 μm²–1 mm². The larger the diamond area is, the more NV centers are present, which leads to a higher overall sensitivity. That results in the flux sensitivities in the $10n\Phi_0$–$10\,\mu\Phi_0$ $(\sqrt{\text{Hz}})^{-1}$ range, while the field sensitivity is in the range from $100\,\text{pT}/\sqrt{\text{Hz}}$ to $100\,\text{fT}/\sqrt{\text{Hz}}$ [18,60]. Since a NV center is sensitive to the field (not flux), the flux sensitivity can be defined properly only for a well-defined geometry designed for flux sensing. However, an additional benefit of NV centers is their ability to capture the field orientation.

Another promising magnetometry platform is based on trapped ions [61–63]. Trapped ions are capable of measuring ac magnetic fields with frequencies of approximately 15 MHz featuring sensitivity of approximately $10\,\text{pT}/\sqrt{\text{Hz}}$ [61]. Since our operational frequencies are of the order of 1 kHz, it is impossible to compare the sensitivities. Finally, we point out that magnetometers exist in biological systems. For instance, the avian compass allows certain bird species to sense relatively small magnetic fields in a fraction of a millisecond [64]. Assuming that for navigation it is enough to detect about 10% of the value of earth's magnetic field, the bird's "sensitivity" would be approximately $50\,\text{nT}/\sqrt{\text{Hz}}$.

As seen from the above comparison between the state-of-the-art platforms, a highly coherent transmon qubit with phase estimation protocol offers a superior flux sensitivity, potentially allowing the level of $1n\Phi_0$ $(\sqrt{\text{Hz}})^{-1}$. In order to push the field sensitivity beyond the commercially available level, engineering of field-capturing components (for example, an integrated pickup loop) is required, which is beyond the scope of the present work.

V. CONCLUSION

In this work we have presented several algorithmic improvements to the Kitaev algorithm using a single qubit and we have considered a multiqubit scheme based on a greedy algorithm. The proposed scheme with N_{qb} qubits is easily implemented since it does not require entanglement and improves the sensitivity by a factor of $1/\sqrt{N_{\text{qb}}}$.

Utilizing IBMQ processors, we have emulated the magnetometry protocol, while strengthening the results with supporting numerical simulations. The results demonstrate that current hardware limitations prevent entangled GHZ states from providing the same level of performance as separate states. However, we anticipate that it may be possible to partially entangle qubits within optimal subsets of a sensitivity-optimized system.

We estimated that increasing the number of transmons up to 100 with $T_2 \sim 1$ ms would improve the sensitivity by two orders of magnitude. We expect that this high coherence time can be maintained while increasing the number of qubits by careful engineering and minimizing the cross coupling. The maximal field range (dynamic range) of the device is associated with the minimal time step to be implemented. Considering state-of-the-art devices with high sampling allowing for 1-ns pulses, we estimate the maximal field range of 2 mT so the phase can be distinguished during QPE. The best resolution is strongly dependent on the coherence time T_2. With $T_2 \sim 200\,\mu$s the final inaccuracy is limited by approximately 10^{-11}–10^{-12} T, as we have shown in the emulation.

The benefit from the increase in the number of qubits and coherence time can be improved by advances in software. According to the results for divergence analysis (in Appendix C), we should consider further improvements of the algorithm for suppressing the difference between the actual and the fastest possible PDF convergence rate. For this purpose, machine learning algorithms can be used; for example, recently they have shown advantage in phase estimation protocols [65].

We have considered measurements of slowly oscillating magnetic fields with approximately 1–10 kHz frequency (defined by T_2). Interestingly, dynamic decoupling techniques are

used for sensing of ac fields [54,66,67], largely eliminating decoherence effects from the $1/f$ noise. In our approach we do not adopt any similar techniques, though it has recently been shown that such schemes should be considered for dc sensing as well [68,69]. Utilization of multilevel artificial atoms theoretically allows for better sensitivity [33,34,70], but coherence of higher transmon levels may be an issue in such strategies.

While we benchmark our protocol using superconducting devices, the described algorithms can be applied to any quantum magnetometry system where the phase is proportional to the measured field and time. Since transmon-based devices feature a low dynamic range and require cryogenic temperatures, other hardware platforms may mitigate such problems. Nevertheless, a comparison to state-of-the-art magnetometers indicates that the transmon qubit is a potential candidate for ultimate sensitivity in quantum magnetometry.

APPENDIX A: PHASE AND AMPLITUDE DAMPING ERRORS

In this Appendix we consider thermal relaxation errors. This error channel is correlated with the amplitude and phase damping error [35] addressed in this Appendix. To connect those two errors, let us write the amplitude damping channel with damping strength $a = 0, \ldots, 1$ in the Kraus form

$$\mathcal{E}(\rho) = E_0 \rho E_0^\dagger + E_1 \rho E_1^\dagger, \tag{A1}$$

where $E_0 = |0\rangle \langle 0| + \sqrt{1-a} |1\rangle \langle 1|$ is the absence of a decay event and $E_1 = \sqrt{a} |0\rangle \langle 1|$ is a decay event; we assume $a = 1 - e^{-t/T_1}$ [71]. Similarly, the phase damping strength parameter $p = 0, \ldots, 1$ can be defined. When the parameters for strength $a, p = 0, \ldots, 1$, are equal to 0, it means that there is no noise in the system.

The parameters a and p change the theoretical probabilities (1) to measure $|0\rangle$ or $|1\rangle$, resulting in $P_{|0\rangle}$ and $P_{|1\rangle}$ approaching 0.5. By increasing a and p we increase the probability of false bit b_k determination. As it was discussed in Sec. II C, in some cases the algorithm can correct itself with further data processing even in the presence of noise and false bit b_k determination. To explore this feature of the algorithm, we monitor the statistics. We introduce the success rate: the
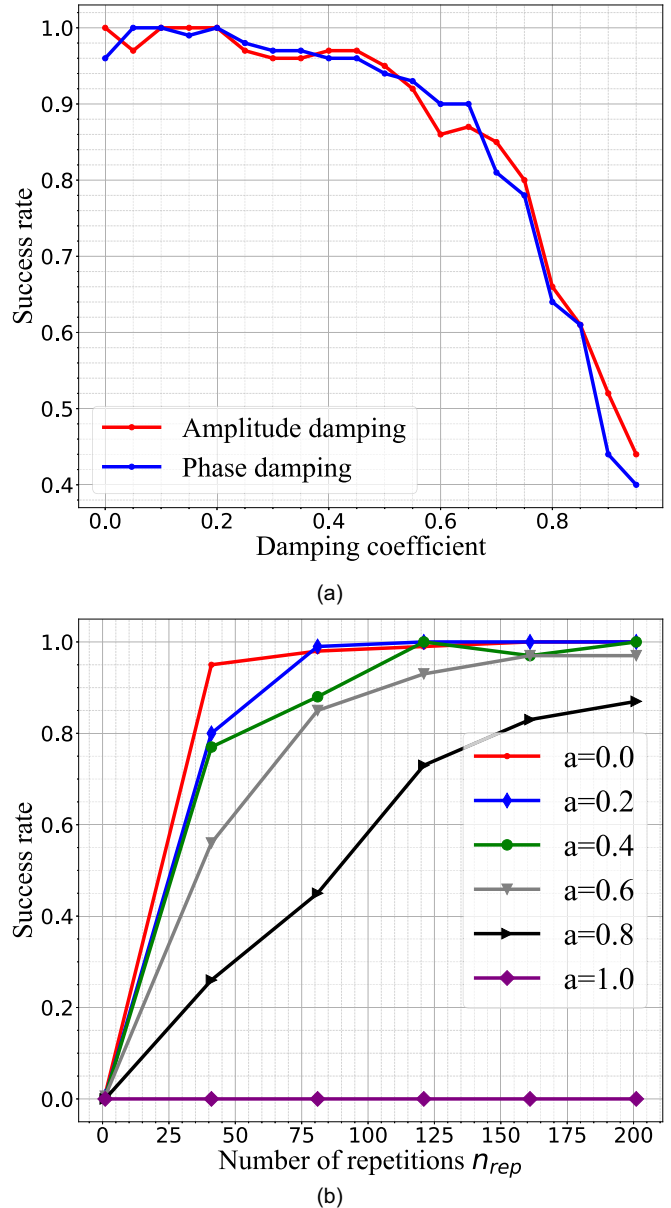

FIG. 7. (a) Success rate under the effect of amplitude and phase damping noises, with $n_{\text{rep}} = 41$. We see that the amplitude and phase noise affect the simulation similarly. (b) Success rate under the effect of different levels of amplitude damping noise a and different $n_{\text{rep}} = 1..201$. It is clear that an increasing n_{rep} increases the success rate for any $a < 1$.

amount of successful performances (when the PDF shrinks to F_c) divided by the total amount of the executions.

We explore how the success rate depends on a and p [see Fig. 7(a)]. The amplitude and phase noise affect the simulation results similarly. Then we optimize n_{rep} by varying amplitude noise levels [see Fig. 7(b)]. For the noiseless system to achieve a success rate of 95% it should be $n_{\text{rep}} = 41$. For an almost 100% success rate it should be $n_{\text{rep}} = 91$. These data can also be applied to further actual device demonstrations. Since in an actual system a and p are always nonzero, we should consider the presence of moderate amplitude-phase damping noise and take the corresponding n_{rep} according to

Fig. [7(b)]. However, increasing n_{rep} also spoils sensitivity A results.

APPENDIX B: UTILIZATION OF THE MULTIQUBIT SCHEME

To simplify the explanation, we assume that we have N_{qb} similar qubits (T_2 and μ of each qubit are the same). We use the fact that $2^{k_{max}-1}t_0 \approx \sum_{k=0}^{k_{max}-2} 2^k t_0$. Indeed, we increase t_k each time twice. Having $k_{max} \sim 10$, we approximate the sum of $t_0, \ldots, t_{k_{max}-2}$ as $t_{k_{max}-1}$. The t_{sum} is minimized when each qubit works approximately the same time. Therefore, each qubit will repeat measurements with time t_k a number $\text{round}\left(\frac{n_{rep}}{N_{qb}}\right)$ of times, where round $(\cdot)$ is the rounding up function. Therefore,

$$t_{sum} \leqslant 2t_{k_{max}-1}\text{round}\left(\frac{n_{rep}}{N_{qb}}\right)$$

$$\leqslant 2t_{k_{max}-1}\left(\frac{n_{rep}}{N_{qb}} + 1\right) \tag{B1}$$

and

$$t_{sum}^{real} \leqslant 2t_{k_{max}-1}\text{round}\left(\frac{n_{rep}}{N_{qb}}\right) + \text{round}\left(\frac{n_{rep}}{N_{qb}}\right)(k_{max}-1)t_p$$

$$\leqslant (2t_{k_{max}-1} + k_{max}t_p)\left(\frac{n_{rep}}{N_{qb}} + 1\right), \tag{B2}$$

where t_{sum} is the sum of all times of interaction and t_{sum}^{real} is the duration of the whole execution, taking into account qubit preparation time t_p, including reset, gates, and readout duration. Thus, for the nonentangled scheme the sum of all interaction times is inversely proportional to the number of qubits $t_{sum} \sim 1/N_{qb}$, which leads to $A \sim \sqrt{t_{sum}} \sim 1/\sqrt{N_{qb}}$.

APPENDIX C: KULLBACK-LEIBLER DIVERGENCE AS A MAGNETOMETRY SUCCESS METRIC

It was discussed in the main text that in a perfect execution case (where all bits b_k are determined correctly) the half-width of the PDF σ and inaccuracy ΔF decrease by factor of 2 per step. From the simulation and emulation results (see Fig. [3]) it can be seen that in an actual emulation σ does not have such perfect scaling. To estimate this imperfection level we introduce the Kullback-Leibler (KL) divergence metric, which has the meaning of an information metric [72]. It compares two probability density functions and yields how different they are. The KL divergence, also known as the relative entropy, is defined as

$$D_{KL}(P||Q) = \sum_{i \in \mathcal{X}} P(i) \log_2 \frac{P(i)}{Q(i)},$$

where P and Q are two probability distributions defined on the same sample space $\mathcal{X}$.

In our case, we expect the algorithm to return a single value F_{pr} which lies within a $\pm(F_{max} - F_{min})/2^{k_{max}}$ segment around F_c. We introduce the normalized uniform distribution under this segment, which is a perfect final theoretical distribution U. One can think of U as an indicator function. A case when
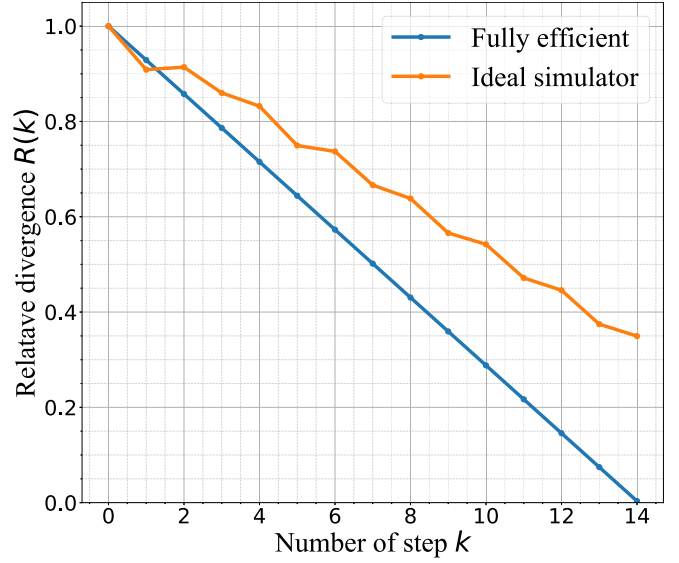

FIG. 8. Relative KL divergence [(C1)] in the information-efficient case (blue) and in the noise-free simulation of sensing (orange). The information efficient case has an exponential decrease of σ and has no error in the determination of F_c. The KL divergence reaches zero since the obtained probability distribution coincides with the target one. The noise-free simulator is not capable of recreating the same dynamics, but the scaling is the same as for the information-efficient case.

the half-width σ decreases by a factor of 2 per step is an ideal PDF evolution. The real evolution of the PDF from emulations might not be that perfect.

We compare the ideal PDF evolution to the one from demonstrations via KL divergence $D_{KL}(\cdot||\cdot)$, using the uniform distribution U as a benchmark. The ideal curve on the kth step is essentially the KL divergence of the uniform distribution and the ideal PDF at step k divided by the initial divergence (KL divergence for $k = 0$) [(C1)]. Thus, the curve is a straight line from 1 to 0, as can be seen in Fig. [8]. Indeed, an exponential decrease of σ and consequently an exponential increase of $P(F_c)$ are linearized by the logarithmic KL divergence [see Eq. [(C1)]].

The corresponding curve from demonstrations against step number k can be obtained by placing the PDF from
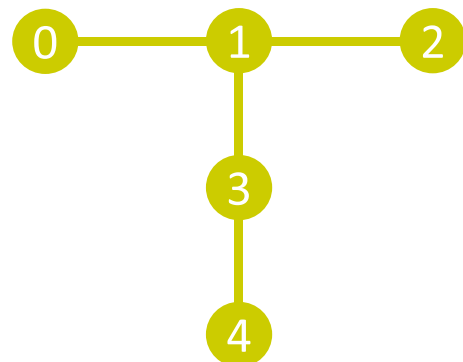

FIG. 9. Connectivity map of the five-qubit IBMQ-Lima device.

demonstrations instead of the ideal into the equation

$$R(k) = \frac{D_{\mathrm{KL}}(U\,\|\,\mathrm{PDF}(k))}{D_{\mathrm{KL}}(U\,\|\,\mathrm{PDF}(k=0))}$$

$$= \frac{\log_2 \frac{1/\Delta F(k_{\max}-1)}{P(F_c)}}{\log_2 \frac{1/\Delta F(k_{\max}-1)}{P_{\mathrm{initial}}(F_c)}}. \tag{C1}$$

We can simplify Eq. (C1) as it is written since U is nonzero at one point of our discrete segment only; this point is F_c. As it can be seen from the equation, in the ideal case $R(k)$ decreases to 0 for the last step indeed. This happens since in the ideal case the final probability $P(F_c)$ is equal to the benchmark probability $1/\Delta F(k_{\max}-1)$ and thus the logarithm is 0.

The algorithm from Sec. III gains information about F_c slower than in the ideal situation of decreasing σ twice each step (see Fig. 8), despite σ following the HL. This means that one can improve the proposed algorithm so it would suppress the information field faster.

APPENDIX D: DETAILED DESCRIPTION OF THE IBMQ-ARMONK PLATFORM

Our magnetometry emulations via IBMQ-Armonk were conducted with the following characteristic parameters: a gate fidelity (Pauli X error) of 2×10^{-4}, characteristic times $T_1 = 160$ μs and $T_2 = 250$ μs, qubit frequency $\nu_0 = 4.97$ GHz, and a frequency of the measurement resonator of 6.99 GHz. The QPU is now one of the retired QISKIT systems [73]. Multiqubit emulations were subsequently conducted on IBMQ-Lima (see Fig. 9 for the connectivity map). This quantum processor had the following characteristics: an average gate fidelity (Pauli X error) of 6×10^{-4}; an average CNOT error of 1×10^{-2}; a median readout error of 3×10^{-2}; average relaxation and coherence times $T_1 = 123$ μs and $T_2 = 101$ μs, respectively; and an average qubit frequency $\nu_0 = 5.2$ GHz. During the experiments on GHZ states, we have to connect a single qubit (target) with all other qubits via CNOT gates and read out its state. For that we use qubit 1 as a target as it has three neighboring qubits and it is easier to couple it with the rest of the multiqubit chip.

[1] R. Zhang, W. Xiao, Y. Ding, Y. Feng, X. Peng, L. Shen, C. Sun, T. Wu, Y. Wu, Y. Yang *et al.*, Recording brain activities in unshielded Earth's field with optically pumped atomic magnetometers, Sci. Adv. **6**, 24 (2020).

[2] R. W. de Gille, J. M. McCoey, L. T. Hall, J.-P. Tetienne, E. P. Malkemper, D. A. Keays, L. C. Hollenberg, and D. A. Simpson, Quantum magnetic imaging of iron organelles within the pigeon cochlea, Proc. Natl. Acad. Sci. USA **118**, e2112749118 (2021).

[3] J.-P. Tetienne, N. Dontschuk, D. A. Broadway, A. Stacey, D. A. Simpson, and L. C. Hollenberg, Quantum imaging of current flow in graphene, Sci. Adv. **3**, e1602429 (2017).

[4] F. Casola, T. Van Der Sar, and A. Yacoby, Probing condensed matter physics with magnetometry based on nitrogen-vacancy centres in diamond, Nat. Rev. Mater. **3**, 17088 (2018).

[5] H. Mamin, M. Kim, M. Sherwood, C. Rettner, K. Ohno, D. Awschalom, and D. Rugar, Nanoscale nuclear magnetic resonance with a nitrogen-vacancy spin sensor, Science **339**, 557 (2013).

[6] K.-M. C. Fu, G. Z. Iwata, A. Wickenbrock, and D. Budker, Sensitive magnetometry in challenging environments, AVS Quantum Sci. **2**, 044702 (2020).

[7] J.-H. Storm, O. Kieler, and R. Körber, Towards ultrasensitive SQUIDs based on submicrometer-sized Josephson junctions, IEEE Trans. Appl. Supercond. **30**, 1600705 (2020).

[8] D. Awschalom, J. Rozen, M. Ketchen, W. Gallagher, A. Kleinsasser, R. Sandstrom, and B. Bumble, Low-noise modular microsusceptometer using nearly quantum limited dc SQUIDs, Appl. Phys. Lett. **53**, 2108 (1988).

[9] F. Wellstood, C. Urbina, and J. Clarke, Hot electron effect in the dc SQUID, IEEE Trans. Magn. **25**, 1001 (1989).

[10] M. Buchner, K. Höfler, B. Henne, V. Ney, and A. Ney, Tutorial: Basic principles, limits of detection, and pitfalls of highly sensitive SQUID magnetometry for nanomagnetism and spintronics, J. Appl. Phys. **124**, 161101 (2018).

[11] C. L. Degen, F. Reinhard, and P. Cappellaro, Quantum sensing, Rev. Mod. Phys. **89**, 035002 (2017).

[12] B. Bao, Y. Hua, R. Wang, and D. Li, Quantum-based magnetic field sensors for biosensing, Adv. Quantum Technol. **6**, 2200146 (2023).

[13] M. A. Nielsen and I. L. Chuang, *Quantum Computation and Quantum Information* (Cambridge University Press, London, 2012).

[14] V. Giovannetti, S. Lloyd, and L. Maccone, Advances in quantum metrology, Nat. Photon. **5**, 222 (2011).

[15] M. Bal, C. Deng, J.-L. Orgiazzi, F. Ong, and A. Lupascu, Ultrasensitive magnetic field detection using a single artificial atom, Nat. Commun. **3**, 1324 (2012).

[16] J. Koch, T. M. Yu, J. Gambetta, A. A. Houck, D. I. Schuster, J. Majer, A. Blais, M. H. Devoret, S. M. Girvin, and R. J. Schoelkopf, Charge-insensitive qubit design derived from the Cooper pair box, Phys. Rev. A **76**, 042319 (2007).

[17] S. Danilin, A. V. Lebedev, A. Vepsäläinen, G. B. Lesovik, G. Blatter, and G. Paraoanu, Quantum-enhanced magnetometry by phase estimation algorithms with a single artificial atom, npj Quantum Inf. **4**, 29 (2018).

[18] R. Katsumi, M. Sekino, and T. Yatsui, Design of an ultrasensitive and miniaturized diamond NV magnetometer based on a nanocavity structure, Jpn. J. Appl. Phys. **61**, 082004 (2022).

[19] J. F. Barry, J. M. Schloss, E. Bauch, M. J. Turner, C. A. Hart, L. M. Pham, and R. L. Walsworth, Sensitivity optimization for NV-diamond magnetometry, Rev. Mod. Phys. **92**, 015004 (2020).

[20] G. Balasubramanian, P. Neumann, D. Twitchen, M. Markham, R. Kolesov, N. Mizuochi, J. Isoya, J. Achard, J. Beck, J. Tissler *et al.*, Ultralong spin coherence time in isotopically engineered diamond, Nat. Mater. **8**, 383 (2009).

[21] E. Herbschleb, H. Kato, Y. Maruyama, T. Danjo, T. Makino, S. Yamasaki, I. Ohki, K. Hayashi, H. Morishita, M. Fujiwara *et al.*, Ultra-long coherence times amongst room-temperature solid-state spins, Nat. Commun. **10**, 3766 (2019).

[22] H. Clevenson, M. E. Trusheim, C. Teale, T. Schröder, D. Braje, and D. Englund, Broadband magnetometry and temperature sensing with a light-trapping diamond waveguide, Nat. Phys. **11**, 393 (2015).

[23] G. De Lange, T. Van Der Sar, M. Blok, Z.-H. Wang, V. Dobrovitski, and R. Hanson, Controlling the quantum dynamics of a mesoscopic spin bath in diamond, Sci. Rep. **2**, 382 (2012).

[24] H. J. Mamin, M. H. Sherwood, M. Kim, C. T. Rettner, K. Ohno, D. D. Awschalom, and D. Rugar, Multipulse Double-Quantum Magnetometry with Near-Surface Nitrogen-Vacancy Centers, Phys. Rev. Lett. **113**, 030803 (2014).

[25] E. Bauch, C. A. Hart, J. M. Schloss, M. J. Turner, J. F. Barry, P. Kehayias, S. Singh, and R. L. Walsworth, Ultralong Dephasing Times in Solid-State Spin Ensembles via Quantum Control, Phys. Rev. X **8**, 031025 (2018).

[26] I. Fescenko, A. Jarmola, I. Savukov, P. Kehayias, J. Smits, J. Damron, N. Ristoff, N. Mosavian, and V. M. Acosta, Diamond magnetometer enhanced by ferrite flux concentrators, Phys. Rev. Res. **2**, 023394 (2020).

[27] C. Zhang, F. Shagieva, M. Widmann, M. Kübler, V. Vorobyov, P. Kapitanova, E. Nenasheva, R. Corkill, O. Rhrle, K. Nakamura *et al.*, Diamond Magnetometry and Gradiometry Towards Sub-picotesla dc Field Measurement, Phys. Rev. Appl. **15**, 064075 (2021).

[28] A. D. Córcoles, M. Takita, K. Inoue, S. Lekuch, Z. K. Minev, J. M. Chow, and J. M. Gambetta, Exploiting Dynamic Quantum Circuits in a Quantum Algorithm with Superconducting Qubits, Phys. Rev. Lett. **127**, 100501 (2021).

[29] A. Y. Kitaev, Quantum measurements and the Abelian stabilizer problem, arXiv:quant-ph/9511026.

[30] M. Perelshtein, A. Sagingalieva, K. Pinto, V. Shete *et al.*, Practical application-specific advantage through hybrid quantum computing, arXiv:2205.04858.

[31] M. Perelshtein, A. Pakhomchik, A. Melnikov, A. Novikov, A. Glatz, G. Paraoanu, V. Vinokur, and G. Lesovik, Solving large-scale linear systems of equations by a quantum hybrid algorithm, Ann. der Physik **534**, 2200082 (2022).

[32] A. Callison and N. Chancellor, Hybrid quantum-classical algorithms in the noisy intermediate-scale quantum era and beyond, Phys. Rev. A **106**, 010101 (2022).

[33] M. R. Perelshtein, N. S. Kirsanov, V. V. Zemlyanov, A. V. Lebedev, G. Blatter, V. M. Vinokur, and G. B. Lesovik, Linear ascending metrological algorithm, Phys. Rev. Res. **3**, 013257 (2021).

[34] A. R. Shlyakhov, V. V. Zemlyanov, M. V. Suslov, A. V. Lebedev, G. S. Paraoanu, G. B. Lesovik, and G. Blatter, Quantum metrology with a transmon qutrit, Phys. Rev. A **97**, 022115 (2018).

[35] Q. D. Team, Qiskit amplitude and phase damping errors (2022).

[36] J. Clarke and A. I. Braginski, *The SQUID Handbook* (Wiley Online Library, 2004), Vol. 1.

[37] J. Clarke and F. K. Wilhelm, Superconducting quantum bits, Nature (London) **453**, 1031 (2008).

[38] R. C. Bialczak, R. McDermott, M. Ansmann, M. Hofheinz, N. Katz, E. Lucero, M. Neeley, A. D. O'Connell, H. Wang, A. N. Cleland, and J. M. Martinis, $1/f$ Flux Noise in Josephson Phase Qubits, Phys. Rev. Lett. **99**, 187006 (2007).

[39] P. Krantz, M. Kjaergaard, F. Yan, T. P. Orlando, S. Gustavsson, and W. D. Oliver, A quantum engineer's guide to superconducting qubits, Appl. Phys. Rev. **6**, 021318 (2019).

[40] T. Chang, T. Cohen, I. Holzman, G. Catelani, and M. Stern, Tunable Superconducting Flux Qubits with Long Coherence Times, Phys. Rev. Appl. **19**, 024066 (2023).

[41] F. Arute, K. Arya, R. Babbush, D. Bacon, J. C. Bardin, R. Barends, R. Biswas, S. Boixo, F. G. Brandao, D. A. Buell *et al.*, Quantum supremacy using a programmable superconducting processor, Nature (London) **574**, 505 (2019).

[42] V. Sevriuk, W. Liu, J. Rönkkö, H. Hsu, F. Marxer, T. Mörstedt, M. Partanen, J. Räbinä, M. Venkatesh, J. Hotari *et al.*, Initial experimental results on a superconducting-qubit reset based on photon-assisted quasiparticle tunneling, Appl. Phys. Lett. **121**, 234002 (2022).

[43] M. D. Reed, B. R. Johnson, A. A. Houck, L. DiCarlo, J. M. Chow, D. I. Schuster, L. Frunzio, and R. J. Schoelkopf, Fast reset and suppressing spontaneous emission of a superconducting qubit, Appl. Phys. Lett. **96**, 203110 (2010).

[44] D. Leibfried, M. D. Barrett, T. Schaetz, J. Britton, J. Chiaverini, W. M. Itano, J. D. Jost, C. Langer, and D. J. Wineland, Toward Heisenberg-limited spectroscopy with multiparticle entangled states, Science **304**, 1476 (2004).

[45] V. Giovannetti, S. Lloyd, and L. Maccone, Quantum-enhanced measurements: Beating the standard quantum limit, Science **306**, 1330 (2004).

[46] V. Giovannetti, S. Lloyd, and L. Maccone, Quantum Metrology, Phys. Rev. Lett. **96**, 010401 (2006).

[47] T. Nagata, R. Okamoto, J. L. O'Brien, K. Sasaki, and S. Takeuchi, Beating the standard quantum limit with four-entangled photons, Science **316**, 726 (2007).

[48] J. P. Dowling, Quantum optical metrology–the lowdown on high-N00N states, Contemp. Phys. **49**, 125 (2008).

[49] S. Danilin and M. Weides, Quantum sensing with superconducting circuits, arXiv:2103.11022.

[50] G. J. Mooney, G. A. L. White, C. D. Hill, and L. C. L. Hollenberg, Generation and verification of 27-qubit Greenberger-Horne-Zeilinger states in a superconducting quantum computer, J. Phys. Commun. **5**, 095004 (2021).

[51] D. Ulam-Orgikh and M. Kitagawa, Spin squeezing and decoherence limit in Ramsey spectroscopy, Phys. Rev. A **64**, 052106 (2001).

[52] F. Fröwis, M. Skotiniotis, B. Kraus, and W. Dür, Optimal quantum states for frequency estimation, New J. Phys. **16**, 083010 (2014).

[53] J. Tang, Y. Zhai, L. Cao, Y. Zhang, L. Li, B. Zhao, B. Zhou, B. Han, and G. Liu, High-sensitivity operation of a single-beam atomic magnetometer for three-axis magnetic field measurement, Opt. Express **29**, 15641 (2021).

[54] T. Wolf, P. Neumann, K. Nakamura, H. Sumiya, T. Ohshima, J. Isoya, and J. Wrachtrup, Subpicotesla Diamond Magnetometry, Phys. Rev. X **5**, 041001 (2015).

[55] A. Somoroff, Q. Ficheux, R. A. Mencia, H. Xiong, R. V. Kuzmin, and V. E. Manucharyan, Millisecond coherence in a superconducting qubit, arXiv:2103.08578 [Phys. Rev. Lett. (to be published)].

[56] C. Wang, X. Li, H. Xu, Z. Li, J. Wang, Z. Yang, Z. Mi, X. Liang, T. Su, C. Yang *et al.*, Towards practical quantum computers: Transmon qubit with a lifetime approaching 0.5 milliseconds, npj Quantum Inf. **8**, 3 (2022).

[57] M. W. Doherty, N. B. Manson, P. Delaney, F. Jelezko, J. Wrachtrup, and L. C. Hollenberg, The nitrogen-vacancy colour centre in diamond, Phys. Rep. **528**, 1 (2013).

[58] R. Schirhagl, K. Chang, M. Loretz, and C. L. Degen, Nitrogen-vacancy centers in diamond: Nanoscale sensors for physics and biology, Annu. Rev. Phys. Chem. **65**, 83 (2014).

[59] N. Wang, C.-F. Liu, J.-W. Fan, X. Feng, W.-H. Leong, A. Finkler, A. Denisenko, J. Wrachtrup, Q. Li, and R.-B. Liu, Zero-field magnetometry using hyperfine-biased nitrogen-vacancy centers near diamond surfaces, Phys. Rev. Res. **4**, 013098 (2022).

[60] J. L. Webb, L. Troise, N. W. Hansen, J. Achard, O. Brinza, R. Staacke, M. Kieschnick, J. Meijer, J.-F. Perrier, K. Berg-Sørensen *et al.*, Optimization of a diamond nitrogen vacancy centre magnetometer for sensing of biological signals, Front. Phys. **8**, 522536 (2020).

[61] I. Baumgart, J.-M. Cai, A. Retzker, M. B. Plenio, and C. Wunderlich, Ultrasensitive Magnetometer using a Single Atom, Phys. Rev. Lett. **116**, 240801 (2016).

[62] M. Wahnschaffe, H. Hahn, G. Zarantonello, T. Dubielzig, S. Grondkowski, A. Bautista-Salvador, M. Kohnen, and C. Ospelkaus, Single-ion microwave near-field quantum sensor, Appl. Phys. Lett. **110**, 034103 (2017).

[63] R. Puebla, Y. Ban, J. F. Haase, M. B. Plenio, M. Paternostro, and J. Casanova, Versatile Atomic Magnetometry Assisted by Bayesian Inference, Phys. Rev. Appl. **16**, 024044 (2021).

[64] Y. Zhang, Z. Hu, Y. Wang, and K. Sabre, Quantum simulation of the radical pair dynamics of the avian compass, J. Phys. Chem. Lett. **14**, 832 (2023).

[65] N. F. Costa, O. Yasser, A. Sultanov, and G. S. Paraoanu, Benchmarking machine learning algorithms for adaptive quantum phase estimation with noisy intermediate-scale quantum sensors, EPJ Quantum Technol. **8**, 16 (2021).

[66] J. M. Taylor, P. Cappellaro, L. Childress, L. Jiang, D. Budker, P. Hemmer, A. Yacoby, R. Walsworth, and M. Lukin, High-sensitivity diamond magnetometer with nanoscale resolution, Nat. Phys. **4**, 810 (2008).

[67] D. Farfurnik, A. Jarmola, D. Budker, and N. Bar-Gill, Spin ensemble-based AC magnetometry using concatenated dynamical decoupling at low temperatures, J. Opt. **20**, 024008 (2018).

[68] A. A. Wood, A. Stacey, and A. M. Martin, DC Quantum Magnetometry below the Ramsey Limit, Phys. Rev. Appl. **18**, 054019 (2022).

[69] A. A. Wood, A. G. Aeppli, E. Lilette, Y. Y. Fein, A. Stacey, L. C. L. Hollenberg, R. E. Scholten, and A. M. Martin, T_2-limited sensing of static magnetic fields via fast rotation of quantum spins, Phys. Rev. B **98**, 174114 (2018).

[70] V. Zemlyanov, N. Kirsanov, M. Perelshtein, D. Lykov, O. Misochko, M. Lebedev, V. Vinokur, and G. Lesovik, Phase estimation algorithm for the multibeam optical metrology, Sci. Rep. **10**, 8715 (2020).

[71] M. A. Nielsen and I. Chuang, *Quantum Computation and Quantum Information*, 10th ed. (Cambridge University Press, Cambridge, 2011).

[72] M. Ma, D. Cheng, S. Chalup, and Z. Zhou, Uncertainty estimation in the neural model for aeromagnetic compensation, IEEE Geosci. Remote Sens. Lett. **15**, 1942 (2018).

[73] Q. D. Team, Retired IBM Quantum systems (2023).